

Amplified linear and nonlinear chiral sensing assisted by anapole modes in hybrid metasurfaces

Cite as: Appl. Phys. Lett. **124**, 251701 (2024); doi: 10.1063/5.0212393

Submitted: 16 April 2024 · Accepted: 8 June 2024 ·

Published Online: 18 June 2024



View Online



Export Citation



CrossMark

Guillermo Serrera, Javier González-Colsa, and Pablo Albellá^{a)}

AFFILIATIONS

Group of Optics, Department of Applied Physics, University of Cantabria, 39005 Santander, Spain

^{a)}Author to whom correspondence should be addressed: pablo.albella@unican.es

ABSTRACT

The interaction between chiral molecules and circularly polarized light is largely influenced by the local optical chirality density. This interaction prompts substantial demand of the design of nanophotonic platforms capable of enhancing such effects across large and accessible volumes. Such a magnification requires nanostructures that provide strong electric and magnetic field enhancements while preserving the phase relation of circular light. Dielectric nanostructures, particularly those able to support resonances, are ideal candidates for this task due to their capacity for high electric and magnetic field enhancements. On the other hand, efficient third harmonic generation requires strong electric field resonances within dielectric materials, a feature often boosted by incorporating plasmonic materials into hybrid systems. In this work, we numerically propose a coupled silicon disk-gold ring system that can exploit the anapole-induced field confinement to provide a broadband magnified circular dichroism under realistic conditions, reaching values up to a 230-fold enhancement. We also demonstrate that this structure can be employed as an efficient third harmonic generator, which, when integrated with chiral media, enables an 800-fold enhancement in circular dichroism. Furthermore, we show that pulsed illumination at intensities up to 10 GW/cm^2 does not induce temperature increments that could potentially damage the samples. These findings suggest that this system can be a promising and versatile approach toward ultrasensitive chiral sensing.

© 2024 Author(s). All article content, except where otherwise noted, is licensed under a Creative Commons Attribution (CC BY) license (<https://creativecommons.org/licenses/by/4.0/>). <https://doi.org/10.1063/5.0212393>

Efficient discrimination of molecular chirality has lately emerged as a critical challenge for the nanophotonics community.^{1–5} Chirality refers to the property whereby an object cannot be superimposed onto its mirror image,^{6–8} meaning that chiral molecules have mirror-image counterparts, referred to as enantiomers.⁹

Although these enantiomers often share similar properties, their chirality plays a vital role in biological interactions.^{10,11} Many bioreceptors are chiral, so the coupling between chiral molecules and bioreceptors is dependent on this handedness, which can lead to different outcomes. For instance, changes in protein chirality are likely responsible for serious health issues such as Parkinson and Alzheimer's diseases.¹² Thus, there is a growing interest in the precise enantiomer identification, especially in the biosciences and the pharmaceutical industry,¹³ where such distinction becomes critical.

Traditionally, enantiomer discrimination have relied on circular dichroism (CD) spectroscopy. These techniques measure the differences in enantiomer absorption under right- and left-handed circularly polarized light (CPL) illumination.⁹ However, since these differences are intrinsically minuscule ($10^{-2} – 10^{-6}$ times the strength of

absorption), this approach requires high sample concentrations and long measure periods to be effective.¹⁴ This challenge has prompted many nanophotonic platforms to overcome these limitations.

As the authors Tang and Cohen demonstrated in their seminal work,^{15,16} the CD effect, expressed as the difference in absorption rates A between the two circular polarizations, can be calculated as

$$CD = A^R - A^L \propto \Im(\kappa)C, \quad (1)$$

where κ is the Pasteur parameter of the chiral medium, accounting for the coupling between electric and magnetic dipoles through the constitutive relations $\mathbf{D} = \epsilon\mathbf{E} - i\kappa\sqrt{\epsilon_0\mu_0}\mathbf{H}$ and $\mathbf{B} = \mu\mathbf{H} + i\kappa\sqrt{\epsilon_0\mu_0}\mathbf{E}$, and C is the optical chirality density (OCD), defined as

$$C = -\frac{\omega\epsilon_0}{2}\Im(\mathbf{E}^* \cdot \mathbf{B}) = -\frac{\omega}{2c^2}|\mathbf{E}||\mathbf{H}|\cos(\Phi), \quad (2)$$

where Φ is the phase angle between $i\mathbf{E}$ and \mathbf{H} . As can be seen from the right-hand side in Eq. (2), for fixed amplitude values of the electric and magnetic fields, OCD is maximized when the fields are collinear and the phase angle Φ is zero, equivalent to a $\pi/2$ phase difference.¹⁷

For plane waves in vacuum, these conditions are both met in circular polarizations, maximizing the OCD to $C_{CPL} = \pm \omega e_0 / 2c|E|^2$. Furthermore, with the use of nanophotonic structures, enhanced optical fields can be engineered to achieve higher values of the OCD if the aforementioned conditions are satisfied.¹⁷

Several approaches to improve chirality detection have come from plasmonics, exploiting the intense local fields created by localized surface plasmon resonances (LSPRs) nearby structures.¹⁸ These resonances induce strong local OCD enhancements, but spatial variations of its sign are often found, leading to negligible spatial averages.¹⁹ Moreover, LSPR excitation in metals, which exhibit resistive losses,^{20,21} usually translates into thermal effects that might damage samples.

On the other hand, OCD enhancement with high refractive index dielectric (HRID) structures is achieved based on both electric and magnetic field enhancements through Mie resonances.^{22–24} This is particularly relevant when these spectrally overlap, as it occurs at the Kerker conditions^{25,26} or in dielectric nanodisks, where resonances can be tuned by manipulating the geometrical aspect ratio.^{27,28} Thus, dual structures with both metal and dielectric materials have led to optimal OCD enhancements.²⁹

Interestingly, HRID structures can also support anapole resonances, characterized by non-radiation and extreme field confinement.³⁰ Anapole modes have been relevant for several applications in nanophotonics,³¹ such as invisibility effects³² or nanolasing.³³ In chiral sensing, anapolar field confinement has been speculated to provide background-free OCD enhancements.³⁴ This has also been exploited for boosting nonlinear optical effects, particularly in third harmonic generation (THG).^{35,36} Specifically, the usage of HRID materials

together with metallic materials has led to very efficient THG in hybrid metastructures.^{37,38}

In this work, we numerically show how a hybrid structure, composed of an HRID (amorphous silicon) holed nanodisk (consisting of a small hollow cylindrical gap located in the center of the silicon disk) coupled to a gold ring, is a promising platform for chiral sensing, providing a broadband high average OCD value across a significant volume. This enhancement comes from the confinement of electric and magnetic energy near anapole resonances, which can also be exploited to provide an enhanced nonlinear third harmonic (TH) CD signal. Moreover, we demonstrate its high thermal tolerance to the illumination conditions needed to generate a significant TH signal without inflicting thermal damage to the sample.

Dielectric disks offer the possibility of tuning their resonances by changing the radius/height aspect ratio. To evaluate the potential of these resonances to enhance chirality, and following the strategy shown in Ref. 34, we perform 3D finite-difference time-domain (FDTD) numerical simulations on amorphous silicon holed disks (material data from Palik³⁹), embedded in water ($n_{Wa} = 1.33$), closely resembling conditions in real experiments.⁴⁰ The choice of amorphous instead of crystalline silicon is based on its nonlinear properties, as amorphous silicon shows significantly lower two-photon absorption while keeping similar optical properties in the infrared range.⁴¹

We set the disk and inner gap radii, $R_{Si} = 300 and $r_{Si} = 25, and explore disk heights from $h = 150 to $h = 510 (corresponding to aspect ratios $h/R_{Si} = 0.5 - 1.7$ in steps of 0.1). In these simulations, the electric and magnetic fields, and$$$$

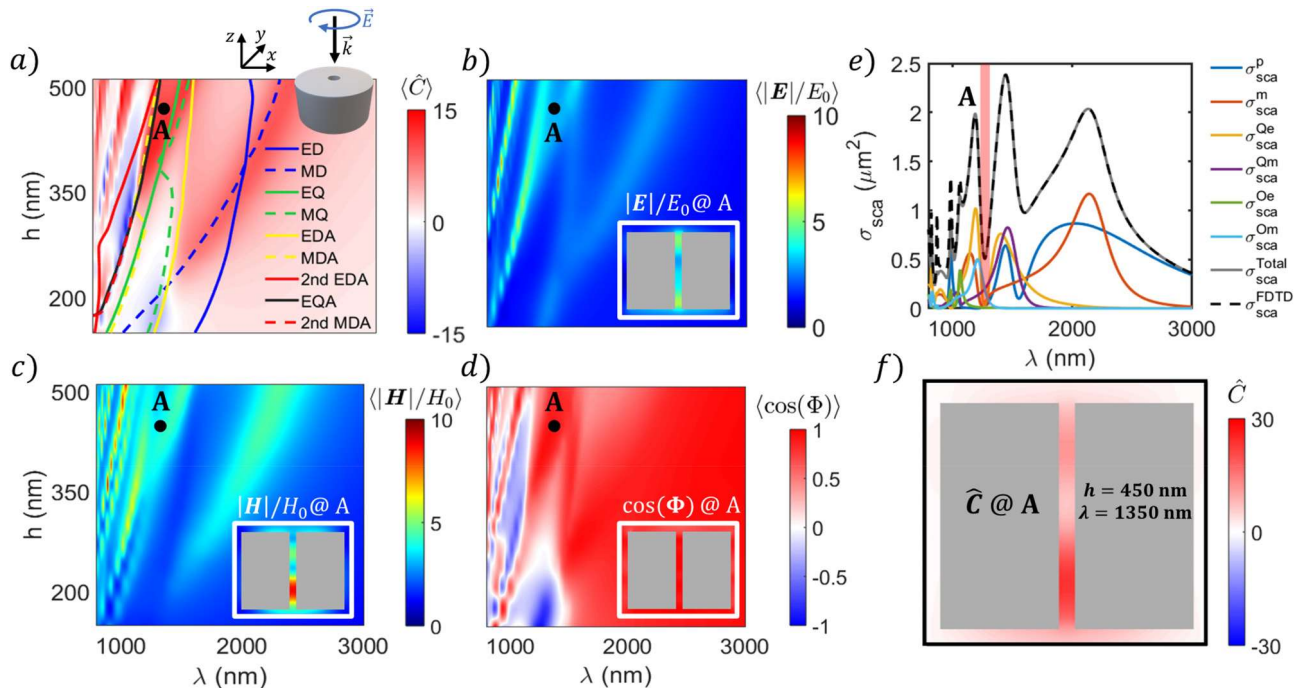


FIG. 1. Evolution of the (a) OCD, (b) electric field, (c) magnetic field enhancements, and (d) phase factor $\cos(\Phi)$ averaged within the inner gap with respect to the disk height and the incident wavelength λ . In (a), marked with solid lines, the evolution of the different resonances can be seen. Insets with spatial distributions in the central xz plane at point A ($h = 450$ nm, $\lambda = 1350$ nm) are shown in (b)–(d). (e) Far field scattering cross section for the $h = 450$ nm case. In red, the spectral position of point A, where anapole resonances overlap, is highlighted. (f) Spatial distribution of the OCD (central xz plane) enhancement at point A.

OCD enhancement \hat{C} within the inner gap are calculated and spatially averaged. Since the mesh size within the gap was uniform, the averaging procedure consisted in a simple arithmetic mean. A far-field multipole decomposition^{42,43} was performed to obtain insight into the evolution of the different resonances with respect to the aspect ratio. These results are summarized in Fig. 1. Scattering cross section results, together with their respective multipole reconstruction, can be found in the [supplementary material](#) (Fig. S1).

Generally, there is a high OCD area [Fig. 1(a)] following the magnetic dipole (MD) resonance, owing to high magnetic field enhancement at that resonance [Fig. 1(c)], together with the electric dipole (ED), which offers a strengthening of the electric field [Fig. 1(b)]. This joint boost of both fields and the phase condition of circular light $\cos(\Phi)$ satisfying Eq. (2) lead to significant OCD enhancement. Additionally, the electric dipole anapole (EDA) mode shows a notable trace of local electric field enhancement, as seen in Fig. 1(b). This finding, and the preservation of the phase condition [Fig. 1(d)], set the basis for our proposal.

The EDA mode, although useful for several purposes, such as nonlinear effect boosting, has a limited utility by itself in terms of OCD. However, when mixed with other strong magnetic resonances, it can provide remarkable conditions for both purposes. This is what is found in the (1200–1400 nm and 350–500 nm) region in Fig. 1(a), with strong OCD averages (up to 15). In this region, there is a significant overlap of several modes, notably the electric quadrupole (EQ), its

anapole (EQA), the magnetic quadrupole (MQ), and a magnetic dipole anapole (MDA) mode [see Fig. 1(e)]. This superposition creates an intense concentration of electric and magnetic fields, which together with a conservation of phase [as seen in Fig. 1(d)] leads to a very strong average OCD. As it can be seen in Fig. 1(f), although this area shows inhomogeneous OCD enhancement, owing to an uneven concentration of magnetic field in the gap, the OCD enhancement sign is unfluctuating.

Calculations for a more realistic system, i.e., considering a high thermal conductivity substrate (amorphous alumina, $n_{Al} = 1.75$), can be found in the [supplementary material](#) (Fig. S2). There, the addition of a substrate causes a mild reduction in the overall enhancement, but the same trends can still be found. For the next step, which consists of adding a gold ring that enhances the nonlinear response while keeping a similar chiroptical response, we choose an optimal size of $h = 450$ nm (aspect ratio $h/R = 1.5$).

After finding an optimal silicon disk configuration, we add gold rings (material properties from Johnson and Christy⁴⁴) to enhance the nonlinear response of the HRID disk while preserving the OCD enhancement. To find an optimal configuration, we explore rings with inner radii $r_{Au} \in [350, 550]$ nm, where the minimum value corresponds to a separation of 50 nm from the silicon disk, and outer radii $R_{Au} \in [400, 750]$ nm. The optimization process consisted on first fixing the inner radius to its minimum value ($r_{Au} = 350$ nm) and changing the outer radius until an optimum point was found. Then, the

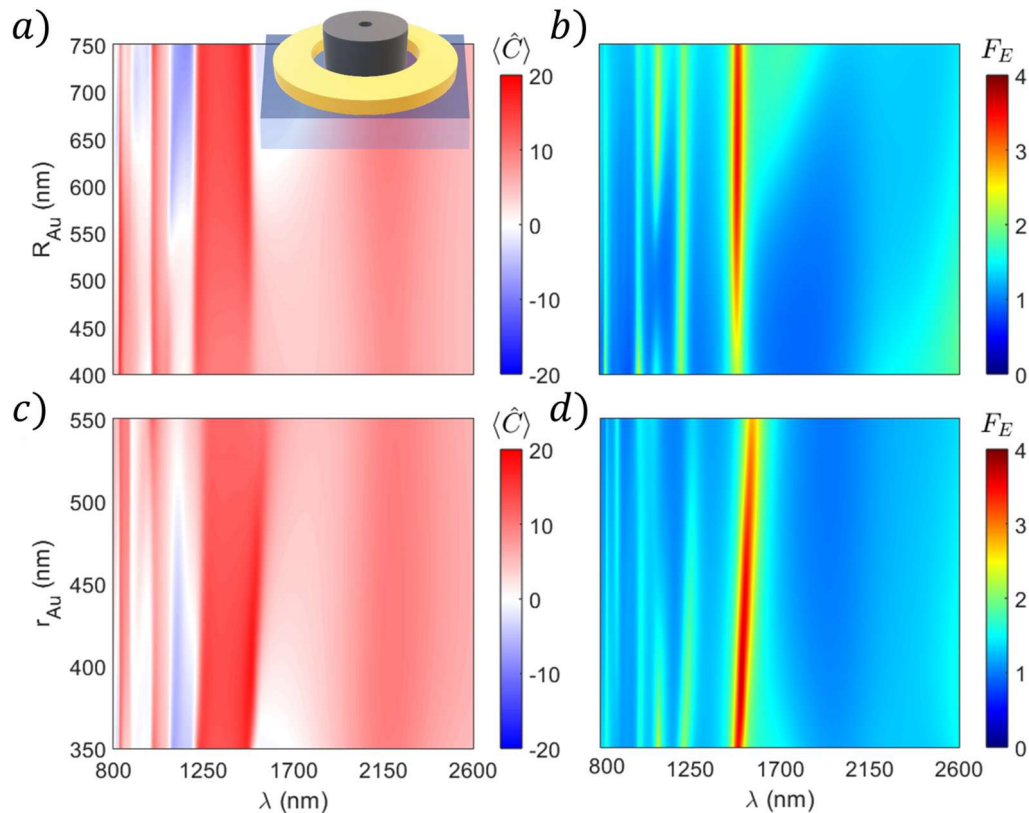


FIG. 2. FDTD results for the gold ring optimization. For a fixed inner radius ($r_{Au} = 350$ nm), (a) OCD and (b) F_E factor inside the silicon disk. For a fixed outer radius ($R_{Au} = 650$ nm), (c) OCD and (d) F_E factor.

same optimization process was applied to the inner radius for the optimal outer radius. The ring height was fixed to $t_{Au} = 100$ nm.

The results for the optimization can be found in Fig. 2(a), where we can see that a high average OCD band (values close to 15) over a relatively broad wavelength range covering from around 1230 to 1500 nm appears. In particular, the outer radius does not affect significantly the overall chirality within this band.

Since the geometry of the gold ring does not seem to significantly affect the chiral properties of the overall structure, we instead focus on optimizing its potential for THG. In order to predict its capabilities, the electric field intensity confined inside the silicon disk is calculated, giving rise to the F_E factor,³⁷

$$F_E = \frac{\iiint |E|^2 dV}{|E_0|^2 V}, \quad (3)$$

where V is the volume of the Si nanodisk. In nanophotonic structures, THG is optimized by maximizing the excitation density, i.e., the electric field intensity. This means that we can predict efficient THG from high values in the F_E factor.

This factor evolution with respect to the incident wavelength and outer radius value can be seen in Fig. 2(b). Two lines corresponding to anapolar resonances (see Sec. SIII in the supplementary material) are found. In particular, the more intense line at 1500 nm, corresponding to the EDA mode, displays a maximum value at $R_{Au} = 650$ nm, marking our optimum value for the first step.

After fixing the outer radius to this value, the ring inner radius is optimized in a similar manner. Figure 2(c) displays analogue results for the OCD average, though reversed, indicating some correlation between OCD and the amount of gold. Focusing again in the F_E factor, in Fig. 3(b), we observe an overall maximum at $r_{Au} = 400$ nm.

After finding an optimal configuration for the structure, we characterize its THG capabilities as well as its thermal behavior, using finite element method (FEM) calculations (COMSOL Multiphysics-RF Module). Scalar third-order nonlinear susceptibilities were applied to gold ($\chi_{Au}^{(3)} = 2 \times 10^{-19} \text{ m}^2/\text{V}^2$) and amorphous silicon ($\chi_{a-Si}^{(3)} = 2.78 \times 10^{-18} \text{ m}^2/\text{V}^2$), consistent with other values found in the literature.³⁸ As the typical values for molecules are several orders of magnitude

lower than those of gold and silicon,⁴⁵ nonlinear optical effects generated within the chiral medium were neglected, thus eliminating the necessity to consider its tensorial character. Simulations were carried out in two steps, following procedures found in previous works.^{46,47} In the first step, electromagnetic fields are calculated for the fundamental frequency under plane wave excitation. To do so, the background plane wave field against the substrate is calculated to serve as input for the scattering problem, which is solved for the complete geometry, considering perfect matched layers (PMLs) across the boundaries of the simulation region. The second step consists in the nonlinear calculations, where the nonlinear polarization term $P_{NL}(3\omega) = \epsilon_0 \chi^{(3)} [E(\omega) \cdot E(\omega)] E(\omega)$ is taken from the fundamental frequency field calculated in the first step. This nonlinear polarization is used as a field source for the second step via an external current excitation $J_{ext} = i3\omega P_{NL}(3\omega)$. Additional details for the thermal analysis can be found in the supplementary material (Sec. SIV), and the results are summarized in Fig. 3.

Figure 3(a) compares the F_E factor with the generated TH signal and average temperature obtained in the FEM simulations. In FEM simulations, mesh size is not uniform at any domain, and therefore, spatial average values were obtained using COMSOL built-in features. A good correlation between the F_E peaks and the integrated TH power P_{TH} is found, except for a small F_E peak at around 1100 nm, which can be associated with the ring ED resonance rather than an anapolar mode. We focus on the peaks at 1220 and 1510 nm, which are of interest as they fall within the high OCD band. The evolution of integrated TH power at those wavelengths with the pump intensity I_0 , going from mild ($0.1 \text{ mW}/\mu\text{m}^2$) to high values ($10^4 \text{ mW}/\mu\text{m}^2$), is shown in Fig. 4(b). Consistently with the F_E factor, the peak at 1510 nm displays higher TH powers. As seen in the figure, both peaks follow the fitted I^3 law, reaching efficiencies $\eta_{THG} = P_{TH}/I_0 \pi R_{Au}^2$ of 0.009% (1220 nm) and 0.088% (1510 nm) at $I = 1 \text{ GW}/\text{cm}^2$. Near field TH profiles at 1220 and 1510 nm are shown in the supplementary material (Fig. S6), suggesting that TH fields radiate toward the substrate at 1220 nm and back to the source at 1510 nm.

Figure 3(a) also shows a good correlation of the average temperature with the anapolar modes where the TH signal is being generated. High Ohmic losses in metals can significantly increase temperature, potentially damaging samples. The high pump intensities required for

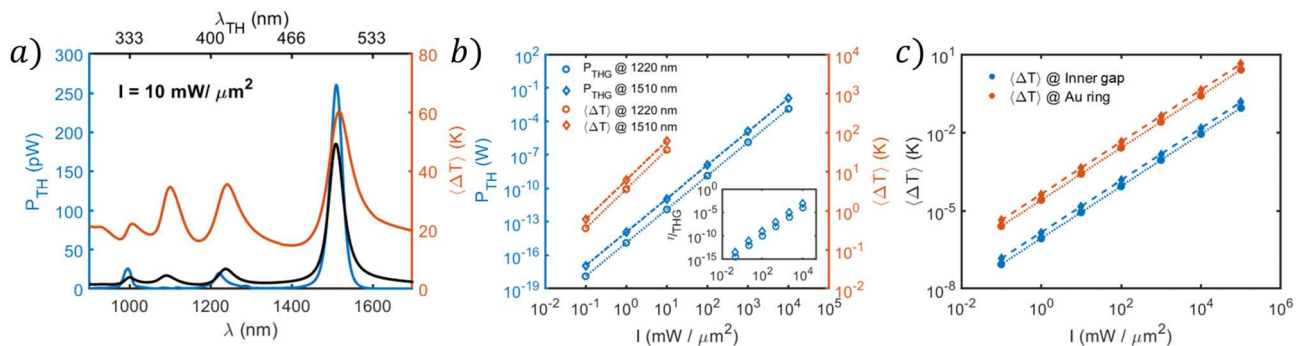


FIG. 3. Results for the nonlinear and thermal analysis. (a) Integrated TH and average temperature spectra compared with F_E^3 (black line), displaying peaks at $\lambda = 1220$ and 1510 nm. (b) Evolution of TH and average temperature maxima under CW illumination for different light intensities, both fitted to cubic and linear functions, respectively. The inset contains the evolution of the THG efficiency η_{THG} with the incident intensity (circles for 1220 nm and diamonds for 1510 nm). (c) Evolution of average temperature maxima (circles for 1220 nm and diamonds for 1510 nm) for different light intensities under femtosecond-pulsed illumination.

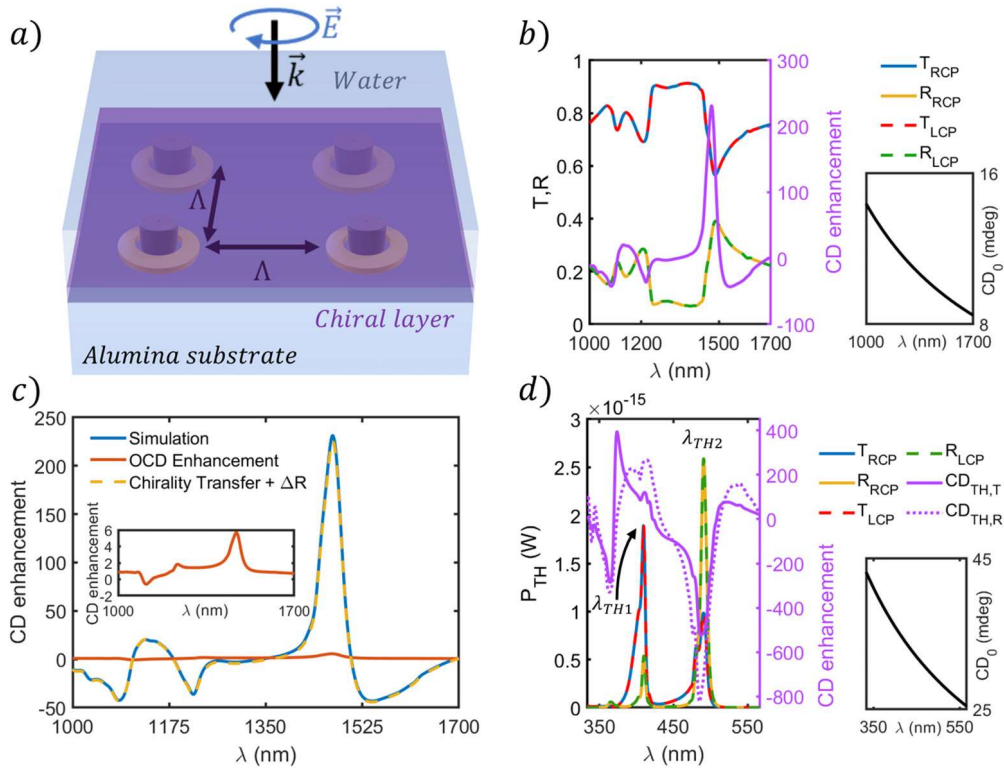


FIG. 4. (a) Scheme of the proposed metasurface. (b) Transmittance and reflectance spectra for the simulated metasurface with RCP and LCP illuminations, as well as the obtained transmission CD enhancement with respect to a bare chiral layer, whose CD signal is shown in the inset. (c) Simulated CD enhancement compared with the theoretical value predicted by OCD enhancement and the contribution from the chirality transfer mechanism. (d) TH integrated power spectra. T refers to integration below the metasurface, and R refers to power integrated above the metasurface. The CD enhancement is shown for both integrations, compared to the transmission CD spectrum of a bare chiral layer at TH frequencies.

nonlinear effects require calculating the maximum temperature rise to ensure sample integrity within a safe intensity range. For continuous wave (CW) illumination, as provided in Fig. 3(b), intensities up to $10 \text{ mW}/\mu\text{m}^2$ were considered, resulting in a maximum temperature increase in 60 K. Since temperatures above 80°C (corresponding approximately to the temperature increment of 60 K from room temperature) typically lead to irreversible protein denaturation,⁴⁸ intensities below this value must be considered to prevent sample damage. A temperature distribution map, valid for both illumination wavelengths, is shown in the supplementary material (Fig. S6).

Although THG usually requires high illumination intensities, and CW illumination has a relatively low intensity threshold for thermal damage, THG typically uses femtosecond lasers with microsecond repetition times, exceeding the cooling time of typical gold nanoparticles in water.⁴⁹ This allows heat dissipation into the high thermal conductivity surrounding media, preventing overheating. Following previous literature, time-dependent heat transfer simulations were carried out in COMSOL assuming typical femtosecond illuminations. The results can be seen in Fig. 3(c), showing the evolution of maximum temperatures with the fluence/intensity. Here, the average temperature increments still follow a linear dependence with fluence/intensity, but the peak values are much lower, so that for all considered intensities (up to $10 \text{ GW}/\text{cm}^2$), no thermal damage is expected.

Finally, to demonstrate the practical functioning of our design, we propose a metasurface design to further illustrate its capabilities to enhance the CD effect. After an optimization process (supplementary material, Sec. SV), we set up a square array with period $\Lambda = 1850 \text{ nm}$ and cover it with a chiral thin layer, representing a sample, with thickness $\delta = 20 \text{ nm}$, characterized by a constant refractive index $n = 1.45 - 0.01i$ and a realistic complex scalar Pasteur parameter $\kappa = 10^{-4} + 10^{-6}i$, owing to the random orientation of molecules.^{1,50} The details of the chiral FEM simulations can be found in the supplementary material (Sec. SVI). Linear and nonlinear CD signals were calculated as

$$CD = \text{atan}\left(\frac{T_R - T_L}{T_R + T_L}\right); \quad CD_{TH} = \text{atan}\left(\frac{P_{R,L}^{3\omega} - P_L^{3\omega}}{P_{R,L}^{3\omega} + P_L^{3\omega}}\right), \quad (4)$$

where $T_{R,L}$ represents the transmittance for either right- or left-handed incident polarizations and $P_{R,L}^{3\omega}$ is the integrated TH power (either in reflection or transmission directions) for the same incidence. Since the CD effect is correlated with the volume of chiral material,³⁴ we increase the radius of the inner gap to $r_{Si} = 50 \text{ nm}$ to place more molecular volume in the high chirality inner gap.

The results for these calculations are summarized in Fig. 4, with the proposed metasurface depicted in Fig. 4(a). Figure 4(b) contains

the calculated linear reflectance and transmittance for both polarizations, as well as the CD effect enhancement $CD_{Enh} = CD/CD_0$ with CD calculated from Eq. (4) and CD_0 being the CD signal from a bare chiral layer covering the substrate, which is shown in the corner inset. The CD_0 signal was calculated analytically using a transfer matrix method approach.⁵⁰ Two peaks (one negative and one positive) can be observed, corresponding to the anapole modes, at both ends of the high transmittance band, with the higher one reaching approximately a 230-fold enhancement.

Figure 4(c) compares the obtained simulation results with the theoretical values given by $CD_{Enh,OCD} = \frac{C}{C_{OCD}}$ ²⁹ and the contribution from the chirality transfer mechanism (differential absorption in the nanostructure as a result of scattering from the chiral medium due to its real part of κ) plus other effects from differential reflection.⁵¹ Here, due to the relationship between the real and imaginary parts of κ (10^2 across all the spectrum), chirality transfer dominates the shape of the signal, particularly at the observed peaks, which correspond to anapole resonances. This can be explained as the field confinement caused by anapole resonances enhances the light-matter interaction in the chiral medium, significantly strengthening the effect. Further discussion, including additional simulation results with a pure imaginary Pasteur parameter and its agreement with theory can be found in the [supplementary material](#) (Sec. SVII).

Finally, Fig. 4(d) shows the results for the conducted nonlinear simulations, including integrated powers above and below the metasurface (similar to reflection and transmittance) for both circular polarizations, as well as the CD effect enhancement. At the first THG wavelength ($\lambda_{TH1} = 410$ nm), transmission dominates for both polarizations, whereas at the second THG wavelength ($\lambda_{TH2} = 490$ nm), reflection prevails. In this case, we find that the CD effect is significantly enhanced at both wavelengths, with 100-fold enhancements compared to the bare chiral film and beyond. In particular, the second THG wavelength showcases an 800-fold enhancement in reflection, suggesting the utility of this metasurface in both transmission (linear CD) and reflection (nonlinear CD) applications.

In conclusion, we have presented a hybrid structure consisting on a holed silicon nanodisk surrounded by a gold ring, achieving a high average OCD and efficient THG. Using FDTD simulations and multipole analysis, we related the high OCD with the spectral overlap of electric and magnetic resonances within the disk's gap, including anapoles. Thermal calculations confirmed no thermal side effects under pulsed illuminations.

To give more insights on the practical functioning of our design, FEM simulations with chiral matter mimicking a real sample were conducted. The proposed metasurface showed up to 230-fold enhancement of the CD effect in transmittance for the linear regime and an 800-fold enhancement in reflectance for the nonlinear TH regime, with a good agreement with theory. We believe that these results lay the foundations toward enhanced measurements of molecular chirality.

See the [supplementary material](#) for the following: results for the scattering cross sections of different aspect ratio silicon holed disks in water with corresponding multipole decompositions; an analysis on the influence of the alumina substrate on the average optical chirality density and multipole analysis; details for the geometrical optimization of the gold ring and multipole analysis; details on thermal FEM

calculations; results for the third harmonic and temperature profiles; the optimization of the metasurface; details on chiral FEM calculations; and a complementary analysis on the chirality transfer mechanism and the differential transmittance and reflectance in metasurfaces, showing compatibility between theory and simulation results.

This work acknowledges funding from the MOPHOSYS Project (No. PID2022-139560NB-I00) from Proyectos de Generación de Conocimiento provided by the Spanish Agencia Estatal de Investigación. G.S. thanks the Spanish Ministry of Education for his predoctoral contract grant (No. FPU21/02296). J.G.-C. thanks the Ministry of Science and Innovation of Spain for his FPI grant (No. PRE2019-088809).

AUTHOR DECLARATIONS

Conflict of Interest

The authors have no conflicts to disclose.

Author Contributions

Guillermo Serrera: Conceptualization (supporting); Formal analysis (lead); Investigation (lead); Methodology (equal); Writing – original draft (lead); Writing – review & editing (equal). **Javier González-Colsa:** Investigation (supporting); Methodology (equal); Writing – original draft (supporting); Writing – review & editing (equal). **Pablo Albella:** Conceptualization (lead); Funding acquisition (equal); Resources (equal); Supervision (equal); Writing – review & editing (equal).

DATA AVAILABILITY

The data that support the findings of this study are available from the corresponding author upon reasonable request.

REFERENCES

- ¹S. Both, M. Schäferling, F. Sterl, E. A. Muljarov, H. Giessen, and T. Weiss, “Nanophotonic chiral sensing: How does it actually work?,” *ACS Nano* **16**(2), 2822–2832 (2022).
- ²M. Hentschel, M. Schäferling, X. Duan, H. Giessen, and N. Liu, “Chiral plasmonics,” *Sci. Adv.* **3**, e1602735 (2017).
- ³A. Lininger, G. Palermo, A. Guglielmelli, G. Nicoletta, M. Goel, M. Hinczewski, and G. Strangi, “Chirality in light-matter interaction,” *Adv. Mater.* **35**(34), 2107325 (2023).
- ⁴M. L. Solomon, A. A. E. Saleh, L. V. Poulikakos, J. M. Abendroth, L. F. Tadesse, and J. A. Dionne, “Nanophotonic platforms for chiral sensing and separation,” *Acc. Chem. Res.* **53**(3), 588–598 (2020).
- ⁵J. Mun, M. Kim, Y. Yang, T. Badloe, J. Ni, Y. Chen, C. W. Qiu, and J. Rho, “Electromagnetic chirality: From fundamentals to nontraditional chiroptical phenomena,” *Light Sci. Appl.* **9**(1), 139 (2020).
- ⁶L. Pasteur, “Mémoire sur la relation qui peut exister entre la forme cristalline et la composition chimique et sur la cause de la polarisation rotatoire,” *C. R. Acad. Sci.* **26**, 535 (1848).
- ⁷W. T. B. Kelvin, *The Molecular Tactics of a Crystal* (Clarendon Press, Oxford, 1894).
- ⁸W. T. B. Kelvin, *Baltimore Lectures on Molecular Dynamics and the Wave Theory of Light* (CJ Clay and Sons, Cambridge, 1904).
- ⁹B. Nordén, *Circular Dichroism and Linear Dichroism* (Oxford University Press, Oxford, 1997).
- ¹⁰S. J. Yoo and Q. H. Park, “Metamaterials and chiral sensing: A review of fundamentals and applications,” *Nanophotonics* **8**(2), 249–261 (2019).

- ¹¹S. Yoo and Q. H. Park, "Chiral light-matter interaction in optical resonators," *Phys. Rev. Lett.* **114**(20), 203003 (2015).
- ¹²C. M. Dobson, "Protein folding and misfolding," *Nature* **426**(6968), 884–890 (2003).
- ¹³K. N. Nina Berova and R. W. Woody, *Circular Dichroism. Principles and Applications*, 2nd ed. (Wiley-VCH, New York, 2000).
- ¹⁴J. S. Choi and M. Cho, "Limitations of a superchiral field," *Phys. Rev. A* **86**(6), 063834 (2012).
- ¹⁵Y. Tang and A. E. Cohen, "Optical chirality and its interaction with matter," *Phys. Rev. Lett.* **104**(16), 163901 (2010).
- ¹⁶Y. Tang and A. E. Cohen, "Enhanced enantioselectivity in excitation of chiral molecules by superchiral light," *Science* **332**(6027), 333–336 (2011).
- ¹⁷M. Hanifeh, M. Albooyeh, and F. Capolino, "Optimally chiral light: Upper bound of helicity density of structured light for chirality detection of matter at nanoscale," *ACS Photonics* **7**(10), 2682–2691 (2020).
- ¹⁸M. Pelton, J. Aizpurua, and G. Bryant, "Metal-nanoparticle plasmonics," *Laser Photonics Rev.* **2**(3), 136–159 (2008).
- ¹⁹A. García-Etxarri and J. A. Dionne, "Surface-enhanced circular dichroism spectroscopy mediated by nonchiral nanoantennas," *Phys. Rev. B* **87**(23), 235409 (2013).
- ²⁰F. Reyes Gómez, O. N. Oliveira, P. Albella, and J. R. Mejía-Salazar, "Enhanced chiroptical activity with slotted high refractive index dielectric nanodisks," *Phys. Rev. B* **101**(15), 155403 (2020).
- ²¹J. González-Colsa, G. Serrera, J. M. Saiz, D. Ortiz, F. González, F. Bresme, F. Moreno, and P. Albella, "Gold nanodoughnut as an outstanding nanoheater for photothermal applications," *Opt. Express* **30**(1), 125–137 (2022).
- ²²A. I. Kuznetsov, A. E. Miroshnichenko, Y. H. Fu, J. Zhang, and B. Lukyanchuk, "Magnetic light," *Sci. Rep.* **2**, 492 (2012).
- ²³B. García-Cámarra, R. Gómez-Medina, J. J. Sáenz, and B. Sepúlveda, "Sensing with magnetic dipolar resonances in semiconductor nanospheres," *Opt. Express* **21**(20), 23007 (2013).
- ²⁴P. Albella, M. A. Poyli, M. K. Schmidt, S. A. Maier, F. Moreno, J. J. Sáenz, and J. Aizpurua, "Low-loss electric and magnetic field-enhanced spectroscopy with subwavelength silicon dimers," *J. Phys. Chem. C* **117**(26), 13573–13584 (2013).
- ²⁵E. Mohammadi, A. Tavakoli, P. Dehkhoda, Y. Jahani, K. L. Tsakmakidis, A. Tittl, and H. Altug, "Accessible superchiral near-fields driven by tailored electric and magnetic resonances in all-dielectric nanostructures," *ACS Photonics* **6**(8), 1939–1946 (2019).
- ²⁶A. I. Barreda, J. M. Saiz, F. González, F. Moreno, and P. Albella, "Recent advances in high refractive index dielectric nanoantennas: Basics and applications," *AIP Adv.* **9**(4), 040701 (2019).
- ²⁷A. B. Evlyukhin, C. Reinhardt, and B. N. Chichkov, "Multipole light scattering by nonspherical nanoparticles in the discrete dipole approximation," *Phys. Rev. B* **84**(23), 235429 (2011).
- ²⁸I. Staude, A. E. Miroshnichenko, M. Decker, N. T. Fofang, S. Liu, E. Gonzales, J. Dominguez, T. S. Luk, D. N. Neshev, I. Brener, and Y. Kivshar, "Tailoring directional scattering through magnetic and electric resonances in subwavelength silicon nanodisks," *ACS Nano* **7**(9), 7824–7832 (2013).
- ²⁹E. Mohammadi, A. Tittl, K. L. Tsakmakidis, T. V. Raziman, and A. G. Curto, "Dual nanoresonators for ultrasensitive chiral detection," *ACS Photonics* **8**(6), 1754–1762 (2021).
- ³⁰A. E. Miroshnichenko, A. B. Evlyukhin, Y. F. Yu, R. M. Bakker, A. Chipouline, A. I. Kuznetsov, B. Luk'yanchuk, B. N. Chichkov, and Y. S. Kivshar, "Nonradiating anapole modes in dielectric nanoparticles," *Nat. Commun.* **6**(1), 8069 (2015).
- ³¹K. V. Baryshnikova, D. A. Smirnova, B. S. Luk'yanchuk, and Y. S. Kivshar, "Optical anapoles: Concepts and applications," *Adv. Opt. Mater.* **7**(14), 1801350 (2019).
- ³²A. A. Basharin, E. Zanganeh, A. K. Ospanova, P. Kapitanova, and A. B. Evlyukhin, "Selective superinvisibility effect via compound anapole," *Phys. Rev. B* **107**(15), 155104 (2023).
- ³³J. S. Totero Gongora, A. E. Miroshnichenko, Y. S. Kivshar, and A. Fratalocchi, "Anapole nanolasers for mode-locking and ultrafast pulse generation," *Nat. Commun.* **8**(1), 15535 (2017).
- ³⁴K. Du, P. Li, H. Wang, K. Gao, R. Bin Liu, F. Lu, W. Zhang, and T. Mei, "Optical chirality enhancement in hollow silicon disk by dipolar interference," *Adv. Opt. Mater.* **9**(5), 2001771 (2021).
- ³⁵G. Grinblat, Y. Li, M. P. Nielsen, R. F. Oulton, and S. A. Maier, "Enhanced third harmonic generation in single germanium nanodisks excited at the anapole mode," *Nano Lett.* **16**(7), 4635–4640 (2016).
- ³⁶L. Xu, M. Rahmani, K. Zangeneh Kamali, A. Lamprianidis, L. Ghirardini, J. Sautter, R. Camacho-Morales, H. Chen, M. Parry, I. Staude, G. Zhang, D. Neshev, and A. E. Miroshnichenko, "Boosting third-harmonic generation by a mirror-enhanced anapole resonator," *Light Sci. Appl.* **7**(1), 44 (2018).
- ³⁷T. Shibamura, G. Grinblat, P. Albella, and S. A. Maier, "Efficient third harmonic generation from metal-dielectric hybrid nanoantennas," *Nano Lett.* **17**(4), 2647–2651 (2017).
- ³⁸Y. Li, G. Zhang, Y. Tang, X. Zhang, W. Cai, Y. Liu, T. Cao, and G. Li, "Third harmonic generation from the gold/amorphous silicon hybrid metasurface," *Nanophotonics* **11**(10), 2245–2251 (2022).
- ³⁹E. D. Palik, *Handbook of Optical Constants of Solids* (Elsevier, Amsterdam, 1985).
- ⁴⁰J. García-Guirado, M. Svedendahl, J. Puigdolls, and R. Quidant, "Enantiomer-selective molecular sensing using racemic nanoplasmonic arrays," *Nano Lett.* **18**(10), 6279–6285 (2018).
- ⁴¹L. Zhang, A. M. Agarwal, L. C. Kimerling, and J. Michel, "Nonlinear Group IV photonics based on silicon and germanium: From near-infrared to mid-infrared," *Nanophotonics* **3**(4–5), 247–268 (2014).
- ⁴²R. Alaei, C. Rockstuhl, and I. Fernandez-Corbaton, "An electromagnetic multipole expansion beyond the long-wavelength approximation," *Opt. Commun.* **407**, 17–21 (2018).
- ⁴³A. B. Evlyukhin, T. Fischer, C. Reinhardt, and B. N. Chichkov, "Optical theorem and multipole scattering of light by arbitrarily shaped nanoparticles," *Phys. Rev. B* **94**(20), 205434 (2016).
- ⁴⁴P. B. Johnson and R. W. Christy, "Optical constants of the noble metals," *Phys. Rev. B* **6**(12), 4370 (1972).
- ⁴⁵I. Rau, F. Kajzar, J. Luc, B. Sahraoui, and G. Boudebs, "Comparison of Z-scan and THG derived nonlinear index of refraction in selected organic solvents," *J. Opt. Soc. Am. B* **25**(10), 1738–1747 (2008).
- ⁴⁶D. A. Smirnova, A. B. Khanikaev, L. A. Smirnov, and Y. S. Kivshar, "Multipolar third-harmonic generation driven by optically induced magnetic resonances," *ACS Photonics* **3**(8), 1468–1476 (2016).
- ⁴⁷D. Hähnel, C. Golla, M. Albert, T. Zentgraf, V. Myroshnychenko, J. Förstner, and C. Meier, "A multi-mode super-Fano mechanism for enhanced third harmonic generation in silicon metasurfaces," *Light Sci. Appl.* **12**(1), 97 (2023).
- ⁴⁸Y. Matsuura, M. Takehira, Y. Joti, K. Ogashara, T. Tanaka, N. Ono, N. Kunishima, and K. Yutani, "Thermodynamics of protein denaturation at temperatures over 100 °C: CutA1 mutant proteins substituted with hydrophobic and charged residues," *Sci. Rep.* **5**(1), 15545–15549 (2015).
- ⁴⁹G. Baffou and H. Rigneault, "Femtosecond-pulsed optical heating of gold nanoparticles," *Phys. Rev. B* **84**(3), 035415 (2011).
- ⁵⁰D. G. Baranov, B. Munkhbat, N. O. Länk, R. Verre, M. Käll, and T. Shegai, "Circular dichroism mode splitting and bounds to its enhancement with cavity-plasmon-polaritons," *Nanophotonics* **9**(2), 283–293 (2020).
- ⁵¹E. Mohammadi, T. V. Raziman, and A. G. Curto, "Nanophotonic chirality transfer to dielectric Mie resonators," *Nano Lett.* **23**(9), 3978–3984 (2023).